

# Paleoinspired Vision: From Exploring Colour Vision Evolution to Inspiring Camera Design

Junjie Zhang

junjie.z2002@gmail.com

Zhimin Zong

The University of Florida

zzong@ufl.edu

Lin Gu

RIKEN AIP, The University of Tokyo

lin.gu@riken.jp

Shenghan Su

Ziteng Cui

The University of Tokyo

Yan Pu

Institute of Vertebrate Paleontology and Paleoanthropology

Zirui Chen

Carnegie Mellon University

ziruiche@andrew.cmu.edu

Jing Lu

Institute of Vertebrate Paleontology and Paleoanthropology

Daisuke Kojima

The University of Tokyo

sdkojima@mail.ecc.u-tokyo.ac.jp

Tatsuya Harada

The University of Tokyo, RIKEN AIP

harada@mi.t.u-tokyo.ac.jp

Ruogu Fang

The University of Florida

ruogu.fang@ufl.edu

## Abstract

*The evolution of colour vision is captivating, as it reveals the adaptive strategies of extinct species while simultaneously inspiring innovations in modern imaging technology. In this study, we present a simplified model of visual transduction in the retina, introducing a novel opsin layer. We quantify evolutionary pressures by measuring machine vision recognition accuracy on colour images shaped by specific opsins. Building on this, we develop an evolutionary conservation optimisation algorithm to reconstruct the spectral sensitivity of opsins, enabling mutation-driven adaptations to more effectively spot fruits or predators. This model condenses millions of years of evolution within seconds on GPU, providing an experimental framework to test long-standing hypotheses in evolutionary biology, such as vision of early mammals, primate trichromacy from gene duplication, retention of colour blindness, blue-shift of fish rod and multiple rod opsins with bioluminescence. Moreover, the model enables speculative explorations of hypothetical species, such as organisms with eyes adapted to the conditions on Mars. Our findings suggest a minimalist yet effective approach to task-specific camera filter design, optimising the spectral response function to meet application-driven demands. The code will be made publicly available*

*upon acceptance.*

## 1. Introduction

*To suppose that the eye with all its inimitable contrivances... could have been formed by natural selection, seems, I freely confess, absurd in the highest possible degree.*

Charles Darwin “The Origin of Species”

Darwin once argued that the idea of natural selection producing the eye ‘can hardly be considered real.’ However, modern biology has revealed that eyes evolved not just once, but at least 40 different times [57]—a finding that may seem even more improbable. The evolution of colour vision is an especially captivating field, as it not only reveals insights into the complex interplay between biology, environment, and adaptation, but also inspires the design of advanced cameras.

As shown in Fig.1, early vertebrates like Myllokunmingiidae and Coccoosteus [60] had tetrachromatic vision thanks to four types of cone opsins around 518 million years ago [70][13]. This trait still persists in their lineages, such as the pouched lamprey and certain tetrapods. Early mammals like Juramaia [44], lost two of their cone opsins and became dichromats, a trait that persists in most

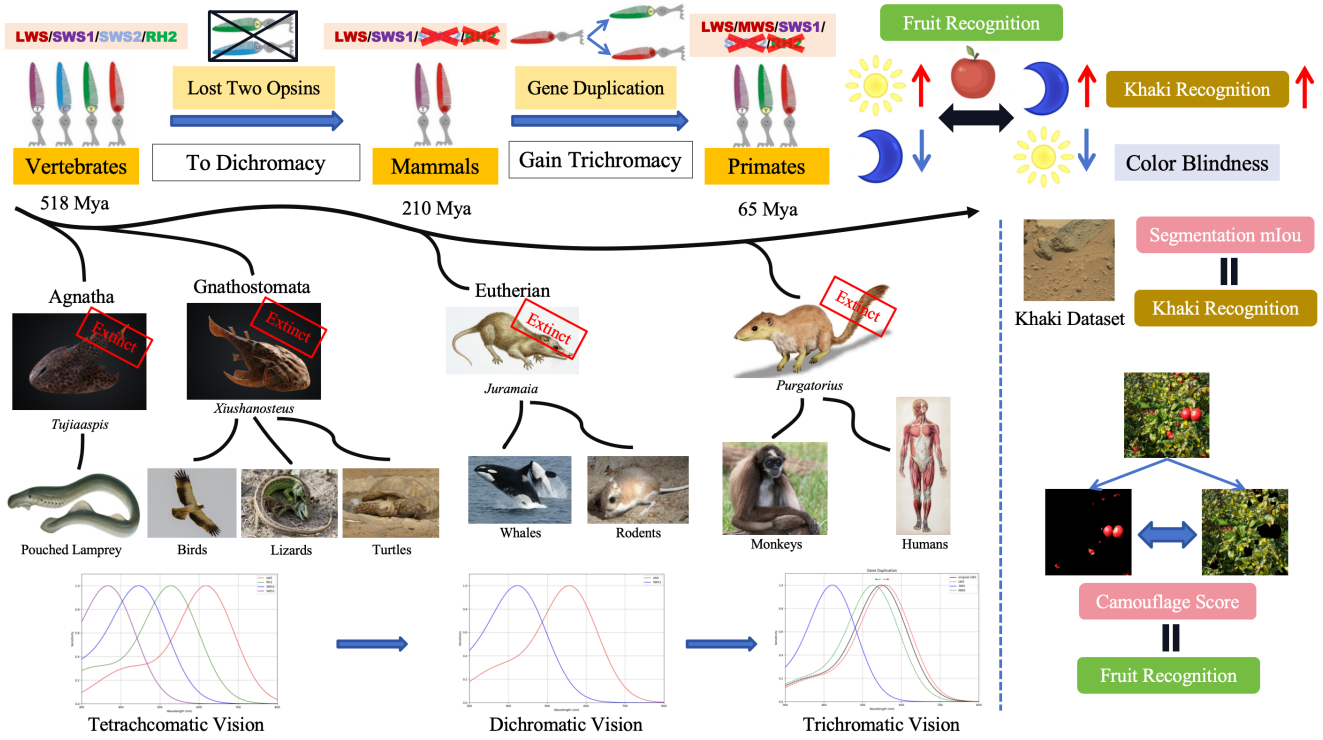


Figure 1. The evolution history from vertebrates to primate lineage.

mammals today, including mice and whales [43][13]. However, approximately 65 million years ago, primates acquired trichromatic vision through a gene duplication event [13][30]. This adaptation passed down through generations including monkeys and humans.

Today, an emerging paradigm called paleoinspired robotics establishes an experimental platform to reconstruct the evolutionary trajectories of both extant and extinct species and quantitatively analyse hypotheses by simplifying of evolutionary processes within traditional robotics framework [28]. Similarly, in this paper, we propose a paleoinspired vision framework called *evolutionary conservation optimisation* to investigate the evolutionary trajectories of colour vision and quantitatively analyse enduring paleontological hypotheses.

As illustrated in Fig.2, colour vision in vertebrates is mediated by opsins in the retina [14], each with a distinct spectral sensitivity function,  $S_c(\lambda)$ , quantifying light detection efficiency across wavelengths. Given the spectral signal at position  $(x, y)$ , represented as  $L(x, y, \lambda)$ , the perceived intensity for each opsin is the integral of its spectral sensitivity over wavelength range, as shown by equation in Fig.2, generating a distinct signal channel for brain. Therefore, we simplify this visual transduction using an *opsin layer* with  $c$  convolutional kernels, where each kernel's weight  $\Psi_c(\lambda)$  represents the spectral sensitivity function. The opsin layer

performs a  $1 \times 1$  convolution operation, which is equivalent to integration above[51], transforming the  $H \times W \times N$  hyperspectral images (HSI) into a size  $H \times W \times C$  feature map (where  $C = 3$  for trichromatic vision). HSI data, collected by hyperspectral cameras[38][6][2], capture the spectral per pixel, where  $N$  represents the number of spectral bands, 400nm, 410nm, and so on. The  $C$  channel maps are then passed to Mix Transformers (MiT) encoder for the consequent recognition task.

Colour vision offers evolutionary advantages, such as the ability to identify ripe, high-energy fruits or detect predators [7][67]. We quantify this advantage by assessing machine recognition performance on images filtered through specific opsins. Specifically, we incorporate a segmentation decoder and optimise(evolve) the spectral sensitivity weights of the opsin layer to enhance the model's mean Intersection over Union (mIoU). This optimisation reflects an improved visual recognition capability, essential for survival in "red in tooth and claw" nature.

However, as shown in Fig.2.c, directly optimising the opsin layer lead to unrestricted spectral sensitivity. This is conflicted with actual evolution for 1. spectral sensitivity function of retinal opsin is generally approximated using Gaussian functions centered at  $\lambda_{max}$  [42][55][22]. 2. mutations in specific amino acid residues in Fig.2.b, also known as spectral tuning sites, typically induce shifts maximum

sensitivity wavelength  $\lambda_{max}$  within a range of 5 nm to 25 nm [71][15]. Therefore, we introduce the *conservative regularisation*, including:

- Parameterising the convolution kernel weights in the opsin layer as a Gaussian function
- Allowing only  $\lambda_{max}$  to change during optimisation
- Limiting shifts in  $\lambda_{max}$  to a maximum of 0.5 nm per epoch

Now we can reconstruct evolution trajectories from vertebrates to primate lineage and provide quantitative analysis for several hypotheses in palaeontology:

- **Vision of early mammals.** We reconstruct the evolutionary transition in mammals from tetrachromatic vision, as seen in vertebrates, to dichromatic vision, driven by the loss of two cone opsins [21].
- **Primate trichromacy from gene duplication.** We reconstruct gene duplication process that enabled primates to evolve from dichromatic to trichromatic vision. We also provide quantitative analysis demonstrating the advantages of trichromatic vision in fruit recognition [12].
- **Retention of colour blindness.** We quantitatively examine the evolutionary advantages of colour blindness over trichromatic vision in tasks like fruit detection under dim light and the identification of dirt and rocks [53][61].
- **Blue-shift of fish rod opsins.** We reconstruct the blue-shift in the maximum sensitivity wavelength of fish rod opsin that occurs with increasing depth, reflecting the adaptation of environments at different depth [72].
- **Multiple rod opsins with bioluminescence.** Researchers have observed that certain deep-sea creatures evolve multiple rod opsins with distinct maximum sensitivity wavelengths in bioluminescent environments [49]. By simplifying environmental conditions, we offer a new perspective to analyse the relationship between bioluminescence and the evolution of multiple rod opsins.

Furthermore, we can even envision hypothetical creatures evolved in Mars.

The proposed framework here can also design spectral response function of sensors for application-specific cameras in Fig.2. We demonstrate this with proof-of-concept designs for:

- **Martian environments.** By improving the segmentation of shadows and rocks on Mars, the designed filters show potential for cameras used in autonomous vehicle navigation in the Martian environment.
- **Cancer detection tasks.** Our design also demonstrates potential for medical-specific cameras capable of detecting abnormal tissue patterns associated with cancer.

The design paradigm grounded in our evolutionary conservation framework is manufacturing-friendly, as each iteration requires only minor adjustments. These changes are easily implementable, enabling rapid updates throughout the production process [63]. Interestingly, the concept

here aligns with the recent minimalist design paradigm [33], which focuses on application-specific cameras with minimal components such as pixels or colour channels. Moreover, it is inherently compatible with human vision, showing potential for use in implantable visual sensors for brain-computer interfaces [50].

In this paper, we present three main contributions:

- We propose a computational framework that integrates opsin layers and evolutionary conservation optimisation to investigate the evolutionary trajectory of opsins.
- We provide an experimental platform designed to reconstruct and quantitatively elucidate evolutionary transitions in colour vision across mammals, primates, and deep-sea creatures.
- We propose a novel minimalist design scheme for task-adaptive cameras that prioritises manufacturing efficiency. Specifically, we tailor the spectral response function of sensors to optimise performance in the Martian environment and for applications in cancer detection.

## 2. Related Works

### 2.1. Paleoinspired Robotics

Advances in paleoinspired robotics have opened new avenues for studying extinct species with limited fossil records [46]. By simulating ancient organisms using robotic platforms, researchers address the challenges of incomplete fossil data [28] by exploring significant transitions in vertebrate locomotion and reconstructing movement patterns of long-extinct species [16, 37]. Integrating robotics with experimental palaeontology yields novel insights into previously unattainable evolutionary trajectories. We extend this concept by utilising evolutionary principles to inform the design of next-generation cameras.

### 2.2. Camera Design

Traditional RGB cameras mimic human colour perception [29] through multiple processing steps [31], but their spectral response functions don't optimise for specific imaging tasks [51]. Deep optics, which combines optics with deep learning [68], has been utilised to design higher-quality cameras [8, 11, 41, 59, 62, 64, 65]. Pre-sensor computing accelerates deep learning computations by focusing on optical neural networks (ONNs). Shi et al. [58] introduced a miniaturized lensless ONN to reduce computational load for incoherent light sources but faced limitations due to shallow layers and lack of nonlinear activation functions. To overcome these issues, a multilayer ONN (MONN) was proposed for pre-sensor optical computing in machine vision [26], processing incoherent light with optical masks and incorporating a quantum dot (QD) film as an all-optical nonlinear activation function [48]. Operating passively without additional energy consumption,

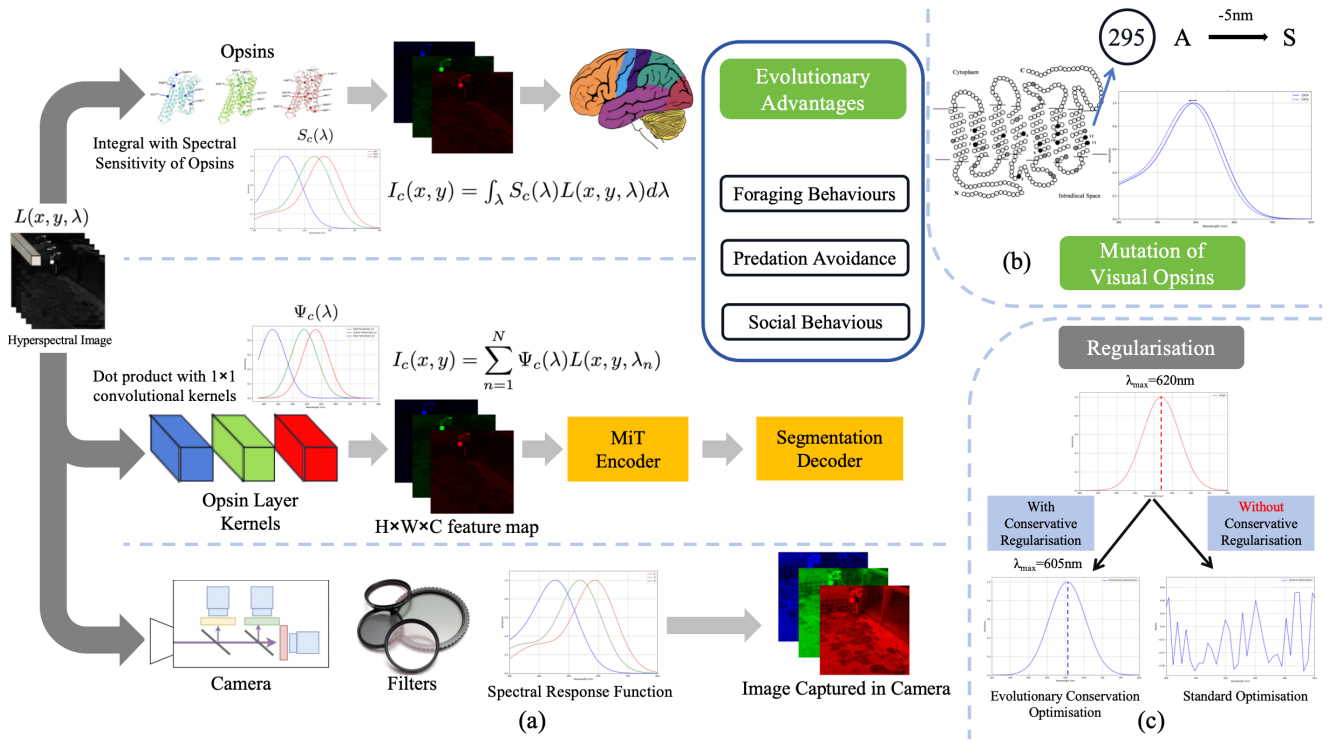


Figure 2. Illustration of evolutionary conservation optimisation.

the MONN enhances computational capacity over single-layer ONNs. Experiments demonstrated the MONN’s superior performance in tasks like hand-drawn figure classification, human action recognition, and cell count classification, highlighting its potential for pre-sensor image processing in real-world scenarios. Klotz and Nayar introduced minimalist vision with freeform pixels [33], utilising fewer, arbitrarily shaped pixels to solve specific vision tasks. By capturing only essential information, these systems are privacy-preserving and self-sustaining. Modeled as the first layer of a neural network, each pixel acts as a photodetector with an optical mask, enabling efficient task-specific vision for applications like indoor space monitoring, lighting estimation, and traffic flow analysis.

### 3. Proposed Approach

In this section, we describe our computational model and evolutionary conservation optimisation framework.

#### 3.1. Opsin Layer

The spectral sensitivity of opsins is commonly approximated using Gaussian functions, with a maximum sensitive wavelength defining their response to light [22][42][55]. Therefore, we proposed a simple yet efficient computational model, namely opsin layer to simulate the spectral sensitivity function shown in Fig.2. Since the integration of spectral

and spectral sensitivity function of opsins equivalents to dot product between entries of the convolution kernel and the hyperspectral data, we introduce a specialized  $1 \times 1$  convolutional layer with  $c$  convolution kernels whose weight is parameterised by a Gaussian function, which acts like the spectral sensitivity of visual opsins.

$$\psi_c \in \left\{ \Psi \mid \Psi = \frac{1}{\sqrt{2\pi}\sigma} e^{-\frac{(\lambda_i - \lambda_{max,c})^2}{2\sigma^2}}, i \in \{0, 1, \dots, N\} \right\},$$

$$c \in \{0, 1, \dots, C\} \quad (1)$$

As shown in Eq.1,  $\psi_c$  denotes the  $c$ -th  $1 \times 1$  convolution kernel weight and  $\lambda_i$  represents the wavelength corresponding to the  $i$ -th channel of HSI.  $\lambda_{max,c}$  is the maximum sensitive wavelength and  $\sigma$  is the standard deviation of the Gaussian function.

#### 3.2. Evolutionary Conservation Optimisation

##### 3.2.1. Loss Function

Fig.2 shows evolutionary pressures and selective forces shaping colour vision arise from factors like food detection, predation avoidance, and social behaviour [7]. Therefore, we employ the segmentation task by utilizing segmentation loss (cross-entropy loss in our work).

### 3.2.2. Conservative regularisation

Amino acid residues, known as spectral tuning sites, significantly influence the maximum spectral sensitivity of opsins [56][15][71]. Therefore, we propose the conservative regularisation, which constrains the optimisation of opsin layer to adjust only the parameter  $\lambda_{max}$ . Since amino acid mutations at spectral tuning sites typically induce shifts in  $\lambda_{max}$  within a range of 5 nm to 25 nm [71][15], we adjust the learning rate to restrict  $\lambda_{max}$  to change to a maximum of 0.5 nm per epoch.

### 3.3. MiT Encoder

Whereas the encoder can adopt any architecture [18][20] to encode the output of opsin layer, we use Mix Transformers (MiT) [69] for its semantic segmentation performance. Specifically, we use the MiT-B0 model as the common encoder. The opsin layer’s output is divided into  $4 \times 4$  patches and then projected into tokens via linear projection to match the required transformer input dimension. As shown in Eq.2, the transformer encoder  $E$  creates a multi-resolution feature map tuple  $\Phi$  ranging from high-resolution coarse feature maps  $\Phi_1$  to low-resolution fine-grained feature maps  $\Phi_4$ .

$$E(Input_i) = \Phi = \{\Phi_1, \Phi_2, \Phi_3, \Phi_4\} \quad (2)$$

In addition, unlike ViT [18] that only generates a single-scale and low-resolution feature map due to the columnar structure [9], the hierarchical-structure of MiT produces CNN-like multi-level feature maps ranging from high-resolution coarse to low-resolution fine-grained [69]. The multi-scale feature map  $\Phi_i$  projected by the encoder has a resolution of  $\frac{H}{2^{i+1}} \times \frac{W}{2^{i+1}} \times C_i$ , where  $i \in \{1, 2, 3, 4\}$  and  $C_{i+1} > C_i$ . Therefore, the MiT offers diverse resolution and scale options, catering to the multi-resolution feature map requirements of various downstream tasks.

### 3.4. Segmentation Decoder

For semantic segmentation task, we utilise a lightweight all-MLP decoder[69] that utilises all of the multi-resolution feature maps  $\{\Phi_1, \Phi_2, \Phi_3, \Phi_4\}$  produced by the encoder. In training stage, under our evolutionary conservation optimisation, we concurrently train the opsin layer, transformer head, and segmentation decoder on a HSI dataset.

## 4. Experimental Platform for Evolution

The number of visual opsins in vertebrate species has undergone two major evolutionary transitions: from four opsins in early vertebrates to two in the mammalian lineage, and from two to three opsins in the primate lineage [5]. Interestingly, colour blindness persists in certain primate populations, raising questions about its evolutionary significance. In contrast, deep-sea creatures adapted to low light often possess only rod opsins [45], with many relying on a single

rod opsin [49]. Shozo *et al.* [72] proposed the maximum sensitive wavelengths  $\lambda_{max}$  of rod opsin in squifrelfishes exhibit a blue-shift trend as living depth increases, as shown in Fig.4.a. Interestingly, Musilova *et al.* [49] found that certain deep-sea teleost lineages have independently developed multiple rod opsins.

In this section, we first introduce the datasets utilised in our experiments (Sec.4.1.1 and Sec.4.1.2) and describe the dim-light noise model (Sec.4.1.3). Then we reconstruct the evolutionary transition of mammal lineage (Sec.4.2) and primate lineage (Sec.4.3). Additionally, we provide quantitative analysis for hypotheses about the advantage of colour blindness over normal trichromatic vision (Sec.4.4). Next, we reconstruct the blue-shift phenomenon in squifrelfishes and provide quantitative analysis under certain assumptions for hypotheses of the development of multi rod opsins in deep-sea (Sec.4.5). Finally, we perform predictions of colour vision for hypothetical creatures adapted to Martian environment (Sec.4.6).

## 4.1. Data Preparation

### 4.1.1. Datasets

- **LIB-HSI** [23] contains hyperspectral reflectance images and their corresponding RGB images of building façades in a light industrial environment.
- **MinneApple** [27] consists of a variety of apple tree species. We selected red fruits and cropped a portion of the images that contain only leaves and fruits.
- **VOC2012** [19] is an image segmentation dataset with 20 object classes, such as "person", "car", "dog".
- **Mars-Seg** [40] is a comprehensive collection of images showcasing diverse Martian landscapes. The images taken by Curiosity rover have been downsampled to a resolution of  $560 \times 500$  pixels using bilinear interpolation.

### 4.1.2. HSI Generation

Due to lack of HSI datasets, we reconstruct HSI data from RGB using the method in [6] for MinneApple, VOC2012, and Mars-Seg. This enables modelling the spectral sensitivities of photoreceptor cells in various real-world situations.

### 4.1.3. Noise of Eyes in Dim-Light Environment

We simulate dim-light environments in Sec.4.2, Sec.4.4 and Sec.4.5 by adding a noise layer after opsin layer. We simplify the noise in eye as the Poisson fluctuations of dark light [17][35]. The variance of noise  $\sigma_N^2$  is shown in Eq.3, where  $I$  is the intensity of dark light and  $\tau$  is the noise factor. We referred the value of the signal-to-noise ratio (SNR) under dim light for single cone cell in human and rod cell in macaque monkeys measured by and H.Richard Blackwell [3] and D.M.Schneeweis *et al.* [54] correspondingly, hence set the noise factor  $\tau = 0.1$  for cone cells in Sec.4.2, Sec.4.4

and  $\tau = 0.02$  for rod cells in Sec.4.5.

$$\sigma_N^2 = \tau \times I \quad (3)$$

## 4.2. Evolutionary Transition from Vertebrates to Mammalian Lineage

Table 1. Evolution of mammals under dim light.

Epoch	$\lambda_{1max}$	$\lambda_{2max}$	mIou %
0	620.00	375.00	-
100	610.66	394.75	13.99
200	606.38	406.88	17.51
300	602.59	415.67	18.43
400	599.16	423.27	19.25
500	595.97	431.09	19.39
Eutheria	530-565	420-440	-

Ancestral mammalian species lost all but two visual opsin genes during evolution [13]. For simplicity, we consider the specific maximum sensitive wavelengths of the four cone opsins found in teleosts, which are 620 nm, 530 nm, 450 nm, and 375 nm [5]. In particular, marsupials and eutherians—lineages that led to modern primates—lost the MWS and SWS2 opsin genes, with  $\lambda_{max}$  at 530 nm and 450 nm, respectively [71]. To model this, we train the opsin layer with two convolutional kernels, representing the mammalian opsins, using the processed LIB-HSI dataset to simulate dim-light conditions. As shown in Tab.1, the observed changes in the maximum sensitive wavelengths of opsins align with the expected evolutionary pattern of mammals in dim-light environments.

## 4.3. Evolutionary Transition from Mammalian Lineage to Primate Lineage

The acquisition of trichromatic vision in early mammals is thought to have provided a selective advantage for detecting fruits and tender leaves in a diurnal lifestyle [12], with camouflage detection being a critical aspect of this ability [34]. Inspired by the work of Lamdouar et al. [36], we utilize the camouflage score as a quantitative metric to assess recognition ability for fruits in leaves, with details provided in Supplementary Material Sec.7.2. This score is applied to the MinneApple dataset, where segmentation masks separate red fruits from the background of leaves as shown in Fig.1. A higher camouflage score indicates that the fruit is more effectively camouflaged by the leaves, making it more difficult to recognize.

To simulate dichromatic and trichromatic vision, we utilise an opsin layer comprising three kernels with maximum sensitivity wavelengths  $\lambda_{max}$  of 425, 540, 580 nm, producing a three-channel output for trichromatic vision. For dichromatic vision, we zero out one of the channels, reducing the model to two functional channels. We then compute the camouflage score for both simulations to compare

the fruit recognition capabilities. As shown in Tab.2, we quantitatively explain that trichromatic vision outperforms dichromatic vision in recognizing fruits among leaves.

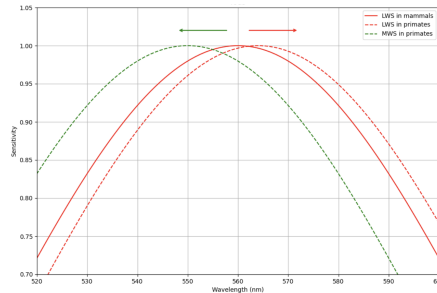


Figure 3. Reconstruction of the gene duplication process in primates.

We also independently reconstruct the process of evolving trichromatic vision from dichromatic vision through gene duplication. It is hypothesized that opsins with maximum sensitivities of 540 and 580 nm originated from a single ancestral gene through duplication [30]. Using the LIB-HSI dataset, which simulates the diurnal environment of primates, we train the opsin layer with initial  $\lambda_{1max}$ ,  $\lambda_{2max}$ , and  $\lambda_{3max}$  at 560, 560, and 425 nm, respectively. During training, we fix  $\lambda_{3max}$  and update only  $\lambda_{1max}$  and  $\lambda_{2max}$  to model the gene duplication process. As illustrated in Fig.3, we successfully reproduce the evolutionary shift in maximum sensitivity wavelengths from dichromatic to trichromatic vision through gene duplication.

## 4.4. Colour Blindness: Advantage of Dichromacy over Trichromacy

The retention of colour blindness in primates may be due to certain evolutionary advantages of dichromatic vision in certain environments. In dim light, dichromatic vision is hypothesised to perform better on fruit recognition [12], potentially providing evolutionary advantage in dim-light situations. In addition, colour blindness may contribute to recognise differences between shades of khaki [4], which probably help colour-blind individuals identify potential food amidst rocks and dirt [61][4]. Our model here quantitatively verifies two hypothesis.

First, we apply the MinneApple dataset and the camouflage score to assess the fruit recognition capabilities of colour-blind individuals compared to those with normal vision. To simulate dim-light situation, we apply the noise layer (Sec.4.1.3) and reduce the original hyperspectral image data by factors of 0.1 and 0.05. To simulate colour blindness, we modify the corresponding opsin layer channels. For example, we set the "R" channel to 0 to simulate red-blindness or apply an attenuation factor to simulate red-weakness. As shown in Tab.3, we quantitatively explain that the ability to detect fruits of colour weakness is better than

Table 2. The comparison of the recognition ability of fruit.

	di-vision	tri-vision
$S_R$	0.2195	0.3161

Table 4. Results of khaki colour recognition.

	colour blindness	normal vision
mIoU %	41.01	40.75

that of normal trichromatic vision under dim light.

Next, we use the Mars-Seg dataset, which contains rocks and dirt in khaki colours as shown in Fig.1, to explore the advantage of colour blindness over normal vision in recognizing khaki colours. As shown in Tab.4, colour blindness exhibits superior segmentation performance compared to normal trichromatic vision, suggesting a potential evolutionary advantage for detecting food in environments filled with rocks and dirt.

#### 4.5. Deep Sea Creatures

In this section, we first provide quantitative analysis for the blue-shift trend in squirrelfishes (Sec.4.5.1). Secondly, we reconstruct the development of multi rod opsins under specific simplification of the bioluminescence (Sec.4.5.2).

It is worth mentioning that in this section we simulate underwater data by pre-processing the LIB-HSI dataset [23][39]. Specifically, we utilise the spectrum of ambient light  $E$  in Eq.4 to reduce the intensity distribution of 204 channels based on different wavelengths. Therefore, we simulate the underwater spectrum and intensity of ambient at different depths.

$$E(d, \lambda) = E(0, \lambda)e^{-K_d(\lambda)d} \quad (4)$$

Here,  $d$  represents the depth,  $\lambda$  is the wavelength,  $E(d, \lambda)$  is the ambient light spectrum at depth  $d$ , and  $E(0, \lambda)$  represents the spectrum at the sea surface.  $K_d(\lambda)$  is diffuse downwelling attenuation [1]. Additionally, we apply the noise layer (Sec.4.1.3) to account for the dim-light conditions typical of underwater environments.

##### 4.5.1. Blue-shift in Rod Opsin of Squirrelfishes

As shown in Fig.4.a, Shozo *et al.* [72] found that the rod opsins of nine squirrelfishes, whose maximum sensitive wavelengths  $\lambda_{max}$  vary between 481 and 502 nm depending on their living depth, share a common ancestral opsin with  $\lambda_{max}$  493 nm. The maximum sensitive wavelengths  $\lambda_{max}$  of rod opsins in squirrelfishes exhibit a blue-shift trend as the living depth increases, as illustrated in Fig.4.b.

Table 3. The comparison of the recognition ability of fruit for normal trichromatic vision and four different kinds of colour blindness.

$S_R$	normal	green-blind	red-blind	green-weak	red-weak
Bright	0.2195	0.3161	0.3334	0.2543	0.2366
Dark(0.1)	0.3093	0.3913	0.3653	0.2927	0.2784
Dark(0.05)	0.3553	0.4200	0.3970	0.3243	0.3241

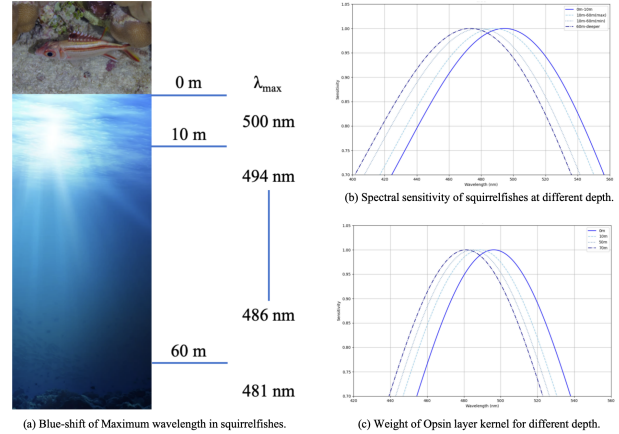


Figure 4. Blue-shift.

Using the processed LIB-HSI dataset [23] adjusted according to Eq.4, representing depths of 0m, 10m, 50m, and 70m, we perform a semantic segmentation task by applying the opsin layer with a single kernel to simulate a single rod opsin. Initial parameter  $\lambda_{max}$  is set to 493 nm, representing the maximum sensitivity of the ancestral rod opsin in squirrelfishes [72].

In quantitative analysis as illustrated in Tab.5, we record the  $\lambda_{max}$  that maximize the mIoU for segmentation on test set for each depth. The maximum sensitive wavelength  $\lambda_{max}$  has an obvious reduction as the depth increases. Therefore, as shown in Fig.4.c, we reconstruct the blue-shift phenomenon in rod opsins in deep-sea, and also quantitatively prove that the cause of the blue-shift phenomenon in squerrelfishes is the diffusion of light in deep-sea.

Table 5. The blue-shift of  $\lambda_{max}$  at different depth.

Depth	$\lambda_{max}$	mIoU %
0m	496.19	30.38
10m	488.73	25.88
50m	484.69	16.97
70m	481.10	14.98

##### 4.5.2. Multi Rod Opsins: Result of Bioluminescence

Except for deep-sea creatures with single rod opsin, Musilova *et al.* [49] found that some of the deep-sea teleost

lineages have independently developed their rod opsins, which mean those lineages have more than one rod opsins in the retina. An explanation for the development of multi rod opsins is the bioluminescence in the specific living environment [49].

As shown in Supplementary Material Sec.8.1, we model the deep-sea environment with bioluminescence by preserving specific regions unaffected by the diffusion function. Experimental results in Sec.8.1 reveal that, without bioluminescence, rod opsins show no significant separation, whereas bioluminescence leads to a maximum 5 nm separation across 5 wavelengths. Despite this, the separation between rod opsins remains small compared to the statistical variation observed in experimental data, suggesting that the mechanism underlying the development of multiple rod opsins may be more complex than initially assumed. Our model could provide clearer insights into this issue if more detailed and accurate anatomical representations of rod opsins were used in future experiments.

#### 4.6. Colour Vision for Hypothetical Martian Life

We train the opsin layer with different number of kernels to explore the colour vision of hypothetical creatures on Mars. Due to space limitations, we have placed the experimental results in Supplementary Material Sec.8.2.

### 5. Camera Design

Inspired by the prediction of colour vision adapted to Martian environment (Sec.4.6), we find the study of colour vision evolution can help design camera for specific environment. Inspired by the analogy between camera colour imaging formulation and a convolutional layer [51], we apply our optimisation framework to refine the spectral response functions of colour filters as shown in Fig.2. In this section, we apply our model on two different datasets (Sec.5.1) to design the camera tailored for the Martian environment (Sec.5.2) and cancer detection tasks (Sec.5.3).

#### 5.1. Datasets

- **Mars-Seg** See Sec. 4.1.1.
- **MHSI Choledoch** [74] is a comprehensive collection of microscopy hyperspectral and colour images focused on cholangiocarcinoma, a type of bile duct cancer.

#### 5.2. Camera for Martian Environment

We train the opsin layer on Mars-Seg dataset to optimise the spectral response function of filters for better segmentation efficiency compared to general filters simplified with Gaussian function of different maximum wavelengths 580, 540 and 425 nm. As shown in Tab.6, we provide a better design with three filters. In supplement material (Sec.9.1), we also provide design schemes with different amounts of filters, which holds potential for Mars exploration tasks, such

as enhancing the imaging capabilities of Mars rovers and other exploration vehicles.

Table 6. Camera design for Martian environment.

Camera	$\lambda_{1max}$	$\lambda_{2max}$	$\lambda_{3max}$	mIou %
General	580.00	540.00	425.00	39.15
Design	611.88	522.93	425.90	39.20

### 5.3. Camera for Cancer Detection

Varghese *et al.* [66] explored how the advancement of AI has the potential to enhance patient outcomes, support surgical education, and optimise surgical care. Inspired by this, we apply our evolutionary conservation optimisation framework on MHSI Choledoch dataset to develop a specialised camera for cancer detection.

Table 7. Camera design for cancer detection.

Camera	$\lambda_{1max}$	$\lambda_{2max}$	$\lambda_{3max}$	mIou %
General	580.00	540.00	425.00	53.17
Design	589.69	529.99	432.53	53.55

As shown in Tab.17, by training the opsin layer, we design a camera with three filters that enhances performance in cancer detection tasks, offering potential for specialized medical imaging systems capable of identifying abnormal tissue patterns associated with cancer. In supplement material (Sec.9.2), we also provide design schemes with different amounts of filters.

### 6. Discussion

In this paper, we present a paleoinspired vision framework that models retinal visual transduction and simulates evolutionary transitions of visual opsins. Our framework enables the quantitative analysis of several hypotheses in opsin evolution with computational efficiency. Traditional evolutionary biology involves a substantial amount of stochastic search that, for instance experiments in forward genetics [24], can result in wasted time and resources through the traits that are difficult to observe and quantify. Instead, our evolutionary framework provides algorithmic tools, which can be used in biological researches to reduce time for prediction, to realise processes that incrementally modify elements of creatures over time, such as evolutionary pressure analysis that quantifies the direction and magnitude that specific traits of opsins change in successive generations. In addition, we provide paradigms to quantitatively analyse the evolution of extinct species by simulating the specific conditions and environment under our optimisation framework.

Not only does our framework produce quantitative analysis to paleontological and biological theories, it also cre-



ates new paradigms for evolution of higher-performance cameras for specialized tasks. This design paradigm for filters in camera is manufacturing-friendly since the conservatism of the optimisation supports small, rapid updates and iterations in the industrial production process [63]. Furthermore, our framework adopts a minimalist approach to camera design, utilizing the fewest possible filters with a flexible spectral sensitivity function tailored to specific tasks. This approach aligns with the minimalist vision systems described in [33]. Additionally, our framework provides design solutions that closely mirror human vision, offering significant potential for applications in the rapidly evolving field of implantable visual sensors for brain-computer interfaces [50]. Notably, recent advances in experimental brain-chip implants aimed at restoring vision have received "breakthrough device" designation from the U.S. Food and Drug Administration, underscoring the relevance and potential impact of such technologies [10].

Future research will focus on expanding our framework to incorporate more complex environmental and anatomical variables, enabling deeper analysis of hypotheses in experimental paleontology. Collaborations with material scientists and engineers are planned to prototype and validate the proposed camera designs, ensuring their practicality and effectiveness in real-world applications.

## References

- [1] Derya Akkaynak and Tali Treibitz. Sea-thru: A method for removing water from underwater images. In *2019 IEEE/CVF Conference on Computer Vision and Pattern Recognition (CVPR)*, pages 1682–1691, 2019. 7
- [2] Liheng Bian, Zhen Wang, Yuzhe Zhang, Lianjie Li, Yinuo Zhang, Chen Yang, Wen Fang, Jiajun Zhao, Chunli Zhu, Qinghao Meng, Xuan Peng, and Jun Zhang. A broadband hyperspectral image sensor with high spatio-temporal resolution. *Nature*, 635(8037):73–81, 2024. 2
- [3] H. Richard Blackwell. Contrast thresholds of the human eye. *J. Opt. Soc. Am.*, 36(11):624–643, 1946. 5
- [4] J. M. Bosten, J. D. Robinson, G. Jordan, and J. D. Mollon. Multidimensional scaling reveals a color dimension unique to color-deficient observers. *Current Biology*, 15(23):R950–R952, 2005. 6
- [5] James K. Bowmaker. Evolution of colour vision in vertebrates. *Eye*, 12(3):541–547, 1998. 5, 6
- [6] Yuanhao Cai, Jing Lin, Xiaowan Hu, Haoqian Wang, Xin Yuan, Yulun Zhang, Radu Timofte, and Luc Van Gool. Mask-guided spectral-wise transformer for efficient hyperspectral image reconstruction. In *2022 IEEE/CVF Conference on Computer Vision and Pattern Recognition (CVPR)*, pages 17481–17490, 2022. 2, 5
- [7] Livia S Carvalho, Daniel MA Pessoa, Jessica K Mountford, Wayne IL Davies, and David M Hunt. The genetic and evolutionary drives behind primate color vision. *Frontiers in ecology and Evolution*, 5:34, 2017. 2, 4
- [8] Praneeth Chakravarthula, Jipeng Sun, Xiao Li, Chenyang Lei, Gene Chou, Mario Bijelic, Johannes Froesch, Arka Majumdar, and Felix Heide. Thin on-sensor nanophotonic array cameras. *ACM Transactions on Graphics (TOG)*, 42(6):1–18, 2023. 3
- [9] Zhe Chen, Yuchen Duan, Wenhai Wang, Junjun He, Tong Lu, Jifeng Dai, and Yu Qiao. Vision transformer adapter for dense predictions, 2023. 5
- [10] Devin Coldewey. Neuralink’s ‘breakthrough device’ clearance from fda does not mean it has cured blindness. *Tech Crunch*. 9
- [11] Geoffroi Côté, Fahim Mannan, Simon Thibault, Jean-François Lalonde, and Felix Heide. The differentiable lens: Compound lens search over glass surfaces and materials for object detection. In *Proceedings of the IEEE/CVF Conference on Computer Vision and Pattern Recognition (CVPR)*, 2023. 3
- [12] M. Vorobyev D. Osorio. Colour vision as an adaptation to frugivory in primates. *Royal Society*, 263:593–599, 1996. 3, 6
- [13] WAYNE I. L. DAVIES, SHAUN P. COLLIN, and DAVID M. HUNT. Molecular ecology and adaptation of visual photopigments in craniates. *Molecular Ecology*, 21(13):3121–3158, 2012. 1, 2, 6
- [14] Hugh Davson and Perkins. Human eye, 2024. 2
- [15] SS Deeb. The molecular basis of variation in human color vision. *Clinical Genetics*, 67(5):369–377, 2005. 3, 5
- [16] Richard Desatnik, Zach J. Patterson, Przemysław Gorzelak, Samuel Zamora, Philip LeDuc, and Carmel Majidi. Soft robotics informs how an early echinoderm moved. *Proceedings of the National Academy of Sciences*, 120(46):e2306580120, 2023. 3
- [17] Kristian Donner. Noise and the absolute thresholds of cone and rod vision. *Vision Research*, 32(5):853–866, 1992. 5
- [18] Alexey Dosovitskiy, Lucas Beyer, Alexander Kolesnikov, Dirk Weissenborn, Xiaohua Zhai, Thomas Unterthiner, Mostafa Dehghani, Matthias Minderer, Georg Heigold, Sylvain Gelly, Jakob Uszkoreit, and Neil Houlsby. An image is worth 16x16 words: Transformers for image recognition at scale, 2021. 5
- [19] M. Everingham, L. Van Gool, C. K. I. Williams, J. Winn, and A. Zisserman. The PASCAL Visual Object Classes Challenge 2012 (VOC2012) Results. <http://www.pascal-network.org/challenges/VOC/voc2012/workshop/index.html>. 5
- [20] Haoqi Fan, Bo Xiong, Karttikeya Mangalam, Yanghao Li, Zhicheng Yan, Jitendra Malik, and Christoph Feichtenhofer. Multiscale vision transformers, 2021. 5
- [21] Jacobs GH. Evolution of colour vision in mammals. *Philos Trans R Soc Lond B Biol Sci*, 2009. 3
- [22] VICTOR I. GOVARDOVSKII, NANNA FYHRQUIST, TOM REUTER, DMITRY G. KUZMIN, and KRISTIAN DONNER. In search of the visual pigment template. *Visual Neuroscience*, 17(4):509–528, 2000. 2, 4
- [23] Nariman Habibi, Ernest Kwan, Weihao Li, Christfried Webers, Jeremy Oorloff, Mohammad Ali Armin, and Lars Petersson. A hyperspectral and rgb dataset for building façade

- segmentation. In *Computer Vision—ECCV 2022 Workshops: Tel Aviv, Israel, October 23–27, 2022, Proceedings, Part VII*, pages 258–267. Springer, 2023. 5, 7
- [24] M. Brent Hawkins, Katrin Henke, and Matthew P. Harris. Latent developmental potential to form limb-like skeletal structures in zebrafish. *Cell*, 184(4):899–911.e13, 2021. 8
- [25] Kaiming He, Xiangyu Zhang, Shaoqing Ren, and Jian Sun. Deep residual learning for image recognition. In *Proceedings of the IEEE conference on computer vision and pattern recognition*, pages 770–778, 2016. 3
- [26] Zheng Huang, Wanxin Shi, Shukai Wu, Yaode Wang, Sigang Yang, and Hongwei Chen. Pre-sensor computing with compact multilayer optical neural network. *Science Advances*, 10(30):eado8516, 2024. 3
- [27] Nicolai Häni, Pravakar Roy, and Volkan Isler. Minneapple: A benchmark dataset for apple detection and segmentation, 2019. 5
- [28] Michael Ishida, Fidji Berio, Valentina Di Santo, Neil H. Shubin, and Fumiya Iida. Paleoinspired robotics as an experimental approach to the history of life. *Science Robotics*, 9(95):eadn1125, 2024. 2, 3
- [29] Jun Jiang, Dengyu Liu, Jinwei Gu, and Sabine Süsstrunk. What is the space of spectral sensitivity functions for digital color cameras? In *2013 IEEE Workshop on Applications of Computer Vision (WACV)*, pages 168–179, 2013. 3
- [30] John D. Mollon Kanwaljit S. Dulai, Miranda von Dornum and David M. Hunt. The evolution of trichromatic color vision by opsin gene duplication in new world and old world primates. *Genome Res*, 9(7):629–638, 1999. 2, 6
- [31] Hakki Can Karaimer and Michael S. Brown. A software platform for manipulating the camera imaging pipeline. In *European Conference on Computer Vision (ECCV)*, 2016. 3
- [32] Diederik P. Kingma and Jimmy Ba. Adam: A method for stochastic optimization, 2017. 1
- [33] Jeremy Klotz and Shree K. Nayar. Minimalist vision with freeform pixels. In *Computer Vision – ECCV 2024*, pages 329–346, Cham, 2025. Springer Nature Switzerland. 3, 4, 9
- [34] Xunfa Lai, Zhiyu Yang, Jie Hu, Shengchuan Zhang, Liujuan Cao, Guannan Jiang, Zhiyu Wang, Songan Zhang, and Rongrong Ji. Camoteacher: Dual-rotation consistency learning for semi-supervised camouflaged object detection, 2024. 6
- [35] T. D. Lamb. Sources of noise in photoreceptor transduction. *J. Opt. Soc. Am. A*, 4(12):2295–2300, 1987. 5
- [36] Hala Lamdouar, Weidi Xie, and Andrew Zisserman. The making and breaking of camouflage, 2023. 6, 1
- [37] George V Lauder. Robotics as a comparative method in ecology and evolutionary biology. *Integrative and Comparative Biology*, 62(3):721–734, 2022. 3
- [38] Daoyu Li, Jinxuan Wu, Jiajun Zhao, Hanwen Xu, and Liheng Bian. Spectratrack: megapixel, hundred-fps, and thousand-channel hyperspectral imaging. *Nature Communications*, 15(1):9459, 2024. 2
- [39] Huapeng Li, Wenxuan Song, Tianao Xu, Alexandre Elsig, and Jonas Kulhanek. Watersplating: Fast underwater 3d scene reconstruction using gaussian splatting, 2024. 7
- [40] Jiaojiao Li, Shun Yao Zi, Rui Song, Yunsong Li, Yinlin Hu, and Qian Du. A stepwise domain adaptive segmentation network with covariate shift alleviation for remote sensing imagery. *IEEE Transactions on Geoscience and Remote Sensing*, 60:1–15, 2022. 5
- [41] Zongling Li, Qingyu Hou, Zhipeng Wang, Fanjiao Tan, Jin Liu, and Wei Zhang. End-to-end learned single lens design using fast differentiable ray tracing. *Opt. Lett.*, 46(21):5453–5456, 2021. 3
- [42] Ellis R. Loew. A third, ultraviolet-sensitive, visual pigment in the tokay gecko (gekko gekko). *Vision Research*, 34(11):1427–1431, 1994. *The Biology of Ultraviolet Reception*. 2, 4
- [43] Spencer G. Lucas and Zhexi Luo. Adelobasileus from the upper triassic of west texas: the oldest mammal. *Journal of Vertebrate Paleontology*, 13(3):309–334, 1993. 2
- [44] Zhe-Xi Luo, Chong-Xi Yuan, Qing-Jin Meng, and Qiang Ji. A jurassic eutherian mammal and divergence of marsupials and placentals. *Nature*, 476(7361):442–445, 2011. 1
- [45] Nik Lupše, Fabio Cortesi, Marko Freese, Lasse Marohn, Jan-Dag Pohlmann, Klaus Wysujack, Reinhold Hanel, and Zuzana Musilova. Visual Gene Expression Reveals a cone-to-rod Developmental Progression in Deep-Sea Fishes. *Molecular Biology and Evolution*, 38(12):5664–5677, 2021. 5
- [46] Amos Matsiko. Advancing scientific discovery with the aid of robotics. *Science Robotics*, 9(95):eadt3842, 2024. 3
- [47] Christian Mauer and Dietmar Wueller. Measuring the spectral response with a set of interference filters. In *Digital photography V*, pages 235–244. SPIE, 2009. 3
- [48] Mario Miscuglio, Armin Mehrabian, Zibo Hu, Shaimaa I Azzam, Jonathan George, Alexander V Kildishev, Matthew Pelton, and Volker J Sorger. All-optical nonlinear activation function for photonic neural networks. *Optical Materials Express*, 8(12):3851–3863, 2018. 3
- [49] Zuzana Musilova, Fabio Cortesi, Michael Matschiner, Wayne I. L. Davies, Jagdish Suresh Patel, Sara M. Stieb, Fanny de Busserolles, Martin Malmstrøm, Ole K. Tørresen, Celeste J. Brown, Jessica K. Mountford, Reinhold Hanel, Deborah L. Stenkamp, Kjetill S. Jakobsen, Karen L. Carleton, Sissel Jentoft, Justin Marshall, and Walter Salzburger. Vision using multiple distinct rod opsins in deep-sea fishes. *Science*, 364(6440):588–592, 2019. 3, 5, 7, 8, 2
- [50] Elon Musk. An integrated brain-machine interface platform with thousands of channels. *J Med Internet Res*, 21(10):e16194, 2019. 3, 9
- [51] Shijie Nie, Lin Gu, Yinqiang Zheng, Antony Lam, Nobutaka Ono, and Imari Sato. Deeply learned filter response functions for hyperspectral reconstruction. In *2018 IEEE/CVF Conference on Computer Vision and Pattern Recognition*, pages 4767–4776, 2018. 2, 3, 8
- [52] Olaf Ronneberger, Philipp Fischer, and Thomas Brox. U-net: Convolutional networks for biomedical image segmentation. In *Medical image computing and computer-assisted intervention—MICCAI 2015: 18th international conference, Munich, Germany, October 5-9, 2015, proceedings, part III 18*, pages 234–241. Springer, 2015. 3
- [53] Atsuko Saito, Akichika Mikami, Shoji Kawamura, Yoshikazu Ueno, Chihiro Hiramatsu, Kanthi A. Widadayati, Bambang Suryobroto, Migaku Teramoto, Yusuke

- Mori, Kunitoshi Nagano, Kazuo Fujita, Hika Kuroshima, and Toshikazu Hasegawa. Advantage of dichromats over trichromats in discrimination of color-camouflaged stimuli in nonhuman primates. *American Journal of Primatology*, 67(4):425–436, 2005. 3
- [54] D.M. SCHNEEWEIS and J.L. SCHNAPF. Noise and light adaptation in rods of the macaque monkey. *Visual Neuroscience*, 17(5):659–666, 2000. 5
- [55] Ryan K. Schott, Rayna C. Bell, Ellis R. Loew, Kate N. Thomas, David J. Gower, Jeffrey W. Streicher, and Matthew K. Fujita. Transcriptomic evidence for visual adaptation during the aquatic to terrestrial metamorphosis in leopard frogs. *BMC Biology*, 20(1):138, 2022. 2, 4
- [56] Ryan K Schott, Matthew K Fujita, Jeffrey W Streicher, David J Gower, Kate N Thomas, Ellis R Loew, Abraham G Bamba Kaya, Gabriela B Bittencourt-Silva, C Guilherme Becker, Diego Cisneros-Heredia, Simon Clulow, Mateo Davila, Jr Firneno, Thomas J, Célio F B Haddad, Sunita Janssenswillen, Jim Labisko, Simon T Maddock, Michael Mahony, Renato A Martins, Christopher J Michaels, Nicola J Mitchell, Daniel M Portik, Ivan Prates, Kim Roelants, Corey Roelke, Elie Tobi, Maya Woolfolk, and Rayna C Bell. Diversity and Evolution of Frog Visual Opsins: Spectral Tuning and Adaptation to Distinct Light Environments. *Molecular Biology and Evolution*, 41(4):msae049, 2024. 5
- [57] I. R. Schwab. The evolution of eyes: major steps. the keeler lecture 2017: centenary of keeler ltd. *Eye*, 32(2):302–313, 2018. 1
- [58] Wanxin Shi, Zheng Huang, Honghao Huang, Chengyang Hu, Minghua Chen, Sigang Yang, and Hongwei Chen. Loen: Lensless opto-electronic neural network empowered machine vision. *Light: Science & Applications*, 11(1):121, 2022. 3
- [59] Zheng Shi, Ilya Chugunov, Mario Bijelic, Geoffroi Côté, Jiwoon Yeom, Qiang Fu, Hadi Amata, Wolfgang Heidrich, and Felix Heide. Split-aperture 2-in-1 computational cameras. *ACM Trans. Graph.*, 43(4), 2024. 3
- [60] D.-G. Shu, H.-L. Luo, S. Conway Morris, X.-L. Zhang, S.-X. Hu, L. Chen, J. Han, M. Zhu, Y. Li, and L.-Z. Chen. Lower cambrian vertebrates from south china. *Nature*, 402(6757):42–46, 1999. 1
- [61] Tom Simonite. Colour blindness may have hidden advantages. *Nature*, 2005. 3, 6
- [62] Qilin Sun, Congli Wang, Fu Qiang, Dun Xiong, and Heidrich Wolfgang. End-to-end complex lens design with differentiable ray tracing. *ACM Transactions on Graphics (TOG)*, 40(4), 2021. 3
- [63] Stefan Thomke. Enlightened experimentation: The new imperative for innovation, 2001. 3, 9
- [64] Ethan Tseng, Shane Colburn, James Whitehead, Luocheng Huang, Seung-Hwan Baek, Arka Majumdar, and Felix Heide. Neural nano-optics for high-quality thin lens imaging. *Nature Communications*, 12(1):6493, 2021. 3
- [65] Ethan Tseng, Ali Mosleh, Fahim Mannan, Karl St-Arnaud, Avinash Sharma, Yifan Peng, Alexander Braun, Derek Nowrouzezahrai, Jean-Francois Lalonde, and Felix Heide. Differentiable compound optics and processing pipeline optimization for end-to-end camera design. *ACM Transactions on Graphics (TOG)*, 40(2), 2021. 3
- [66] Chris Varghese, Ewen M. Harrison, Greg O’Grady, and Eric J. Topol. Artificial intelligence in surgery. *Nature Medicine*, 30(5):1257–1268, 2024. 8
- [67] Misha Vorobyev. Ecology and evolution of primate colour vision. *Clinical and Experimental Optometry*, 87(4-5):230–238, 2004. 2
- [68] Gordon Wetzstein, Aydogan Ozcan, Sylvain Gigan, Shanhui Fan, Dirk Englund, Marin Soljačić, Cornelia Denz, David A B Miller, and Demetri Psaltis. Inference in artificial intelligence with deep optics and photonics. *Nature*, 588(7836):39–47, 2020. 3
- [69] Enze Xie, Wenhai Wang, Zhiding Yu, Anima Anandkumar, José M. Álvarez, and Ping Luo. Segformer: Simple and efficient design for semantic segmentation with transformers. *CoRR*, abs/2105.15203, 2021. 5
- [70] Chuan Yang, Xian-Hua Li, Maoyan Zhu, Daniel J. Condon, and Junyuan Chen. Geochronological constraint on the cambrian chengjiang biota, south china. *Journal of the Geological Society*, 175(4):659–666, 2018. 1
- [71] Shozo Yokoyama. Molecular evolution of vertebrate visual pigments. *Progress in Retinal and Eye Research*, 19(4):385–419, 2000. 3, 5, 6
- [72] Shozo Yokoyama and Naomi Takenaka. The Molecular Basis of Adaptive Evolution of Squirrelfish Rhodopsins. *Molecular Biology and Evolution*, 21(11):2071–2078, 2004. 3, 5, 7
- [73] Boxiang Yun, Qingli Li, Lubov Mitrofanova, Chunhua Zhou, and Yan Wang. Factor space and spectrum for medical hyperspectral image segmentation. In *Medical Image Computing and Computer Assisted Intervention – MICCAI 2023*, pages 152–162, Cham, 2023. Springer Nature Switzerland. 3
- [74] Qing Zhang, Qingli Li, Guanzhen Yu, Li Sun, Mei Zhou, and Junhao Chu. A multidimensional choledoch database and benchmarks for cholangiocarcinoma diagnosis. *IEEE Access*, 7:149414–149421, 2019. 8

# Paleoinspired Vision: From Exploring Colour Vision Evolution to Inspiring Camera Design

## Supplementary Material

### 7. Implementation Details

#### 7.1. Layers after Opsin Layer

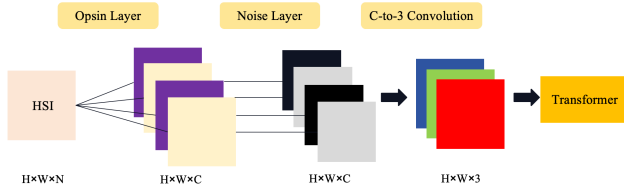


Figure 5. Architecture of the network.

**Noise Layer** The noise layer is applied after each channel of the opsin layer’s output to incorporate the noise present in opsins. Let the output of the opsin layer for channel  $c$  be  $I_c$ ; the output of the noise layer is expressed as:

$$I_c^{noise} = I_c + Gaussian(\mu = 0, \sigma^2 = \tau \times I_c) \quad (5)$$

where  $Gaussian(\mu, \sigma^2)$  represents Gaussian noise with a mean  $\mu$  and variance  $\sigma^2$ , and  $\tau$  is a scaling factor that determines the noise intensity as illustrated in Sec.4.1.3.

**C-to-3 Convolution Layer.** The MiT encoder used in our work requires input data of size  $H \times W \times 3$ , corresponding to a 3-channel image. However, the output of our opsin layer is of size  $H \times W \times C$ , where  $C$  represents the number of convolutional kernels in the opsin layer, corresponding to the simulated number of opsins. To ensure compatibility with the MiT encoder, we introduce a  $1 \times 1$  convolutional layer to transform the feature map from  $H \times W \times C$  to  $H \times W \times 3$ . As shown in Fig.5, this  $1 \times 1$  convolution layer is applied after the opsin layer and the noise layer.

**Training Stage.** In the training stage, we only train the opsin layer and C-to-3 convolution layer (if exist) simultaneously with the encoder and decoder, while fixing the noise layer (if exist).

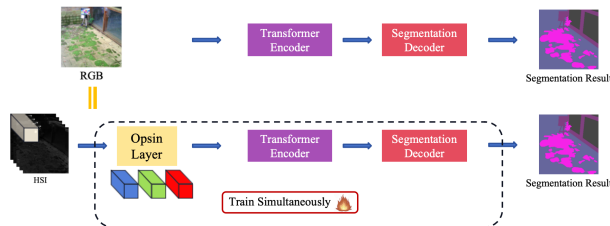


Figure 6. Training stage.

#### 7.2. Camouflage Score

Specifically, we utilize the reconstruction fidelity score proposed by Hala Lamdouar *et al.* [36] as the metric to evaluate the ability of the colour vision to recognize camouflage. For the LMS image  $F$  output from the opsin layer and segmentation mask  $m$ , we first get the foreground region and the background region by erosion and dilation operations on the mask,

$$F_{fg}, F_{bg} = erode(m) \odot F, (1 - dilate(m)) \odot F \quad (6)$$

We calculate the reconstruction fidelity score, which is, briefly, the proportion of pixels in the foreground that can be successfully reconstructed from the background [36],

$$S_R = \frac{1}{N_{fg}} \sum_{(i,j) \in F_{fg}} R_f(i,j) \quad (7)$$

$$R_f(i,j) = \left( \|F_{fg} - \Phi(F_{fg})\|_2 < t \|F_{fg}\|_2 \right) \quad (8)$$

where  $N_{fg}$  is the number of pixels in  $F_{fg}$ ,  $\Phi$  is the reconstruction operation and  $t$  is a threshold parameter. In Sec.4.4, we adjust the value of  $t$  based on the lighting conditions, as  $\|F_{fg}\|_2$  is small in dim light, making the reconstruction criterion for the foreground region more stringent. Specifically, we set  $t = 0.2$  for bright conditions,  $t = 1.2$  for dark(0.1), and  $t = 1.6$  for darker conditions (0.05).

#### 7.3. Training Details

We train the segmentation task on various datasets by minimizing the cross-entropy loss and using the Adam optimizer [32] to update the parameters of the opsin layer, encoder, and decoder.

In training to reconstruct the evolutionary transition to dichromatic vision in mammals (Sec.4.2), we use the Adam optimizer to train the opsin layer with a base learning rate of  $2 \times 10^{-2}$  and the encoder and decoder with a base learning rate of  $5 \times 10^{-4}$ . Additionally, a cosine learning schedule is applied to mitigate over-fitting.

In training to simulate the gene duplication process in primates leading to the acquisition of trichromatic vision (Sec.4.3), we use the Adam optimizer to train the opsin layer with a base learning rate of  $5 \times 10^{-2}$  and the encoder and decoder with a base learning rate of  $5 \times 10^{-4}$ . Additionally, a cosine learning schedule is applied to mitigate over-fitting.

In training to compare the performance of colour blindness and normal trichromatic vision in khaki recognition

Table 8. 1-kernel opsin layer without bioluminescence.

Epoch	$\lambda_{max}$	mIoU %
0	481.00	-
50	471.86	6.69
100	466.09	7.88
150	461.62	10.17
200	457.23	11.14

Table 10. 1-kernel opsin layer with bioluminescence.

Epoch	$\lambda_{max}$	mIoU %
0	481.00	-
50	482.66	8.26
100	482.13	10.09
150	481.41	12.01
200	480.83	15.17

(Sec.4.4), we use the Adam optimizer to train the opsin layer, the encoder and decoder all with a base learning rate of  $5 \times 10^{-4}$ . Additionally, a cosine learning schedule is applied to mitigate over-fitting.

In training to reconstruct the blue-shift phenomenon of rod opsins in squirrelfishes (Sec.4.5.1), we use the Adam optimizer to train the opsin layer with a base learning rate of  $5 \times 10^{-3}$  and the encoder and decoder with a base learning rate of  $5 \times 10^{-4}$ . Additionally, a cosine learning schedule is applied to mitigate over-fitting.

In training to quantitatively analyse the evolutionary development of multiple rod opsins in certain deep-sea species (Sec.4.5.2), we use the Adam optimizer to train the opsin layer with a base learning rate of  $1 \times 10^{-2}$  and the encoder and decoder with a base learning rate of  $5 \times 10^{-4}$ . Additionally, a cosine learning schedule is applied to mitigate over-fitting.

To quantitatively analyse the potential colour vision of hypothetical creatures adapted to Martian environments (Sec.4.6), we use the Adam optimizer to train the opsin layer with a base learning rate of  $5 \times 10^{-2}$  and the encoder and decoder with a base learning rate of  $5 \times 10^{-4}$ . Additionally, a cosine learning schedule is applied to mitigate over-fitting.

For the camera design section (Sec.5), we use the Adam optimizer to train the opsin layer with a base learning rate of  $3 \times 10^{-2}$  and the encoder and decoder with a base learning rate of  $6 \times 10^{-5}$ .

## 8. Supplementary Results for Evolution

### 8.1. Multi Rod Opsins: Result of Bioluminescence

We simulate deep-sea environment with bioluminescence by maintaining the region of a specific label not adjusted by the underwater diffusion, representing a simplified model

Table 9. 5-kernel opsin layer without bioluminescence.

Epoch	$\lambda_{1max}$	$\lambda_{2max}$	$\lambda_{3max}$	$\lambda_{4max}$	$\lambda_{5max}$	mIoU %
0	481.00	481.00	481.00	481.00	481.00	-
50	475.41	475.41	475.26	475.56	475.29	8.44
100	472.89	472.89	472.74	473.04	472.76	12.16
150	470.40	470.38	470.24	470.56	470.26	13.02
200	467.76	467.73	467.59	467.92	467.62	13.77

Table 11. 5-kernel opsin layer with bioluminescence.

Epoch	$\lambda_{1max}$	$\lambda_{2max}$	$\lambda_{3max}$	$\lambda_{4max}$	$\lambda_{5max}$	mIoU %
0	481.00	481.00	481.00	481.00	481.00	-
50	481.78	482.40	480.63	481.46	482.12	10.20
100	481.60	482.53	479.68	481.12	481.76	13.17
150	481.37	482.48	478.96	480.74	481.40	17.67
200	481.73	482.96	478.98	480.98	481.69	21.26

of bioluminescence. As illustrated in Tab.9, rod opsins show no tendency to separate in the absence of bioluminescence. However, under the simulated bioluminescence dataset, as illustrated in Tab.11, under the simulated bioluminescence dataset, the 5 wavelengths in the 5-kernel opsin layer achieve a maximum separation of 5 nm, aligning with the trend observed in the development of multiple rod opsins reported in [49].

This provides quantitative evidence supporting the role of bioluminescence in the development of multiple rod opsins. However, the separation between rod opsins remains minimal compared to biological experimental data [49], aligning with hypotheses suggesting the involvement of more complex mechanisms in the evolution of multiple rod opsins [49].

### 8.2. Colour Vision for Hypothetical Martian Life

In this section, we present predictions of possible colour vision capabilities for hypothetical Martian life, including dichromatic, trichromatic, and tetrachromatic vision.

Firstly, we train a 2-kernel opsin layer to optimize segmentation performance on the Mars-Seg dataset, aiming to predict the optimal dichromatic vision. As shown in Tab.12, the initial wavelengths are set to values similar to human vision, 560 nm and 425 nm.

Secondly, we apply the gene duplication process to the previously trained 2-kernel opsin layer to analyse the evolutionary transition from dichromatic to trichromatic vision adapted to the Martian environment. Specifically, as shown in Tab.13, the initial wavelengths are set to 588.81, 588.81, and 429.37 nm, corresponding to the optimal parameters obtained from the trained 2-kernel layer. It is worth noting that if the low-wavelength-sensitive opsin is allowed to duplicate, no duplication occurs, or more specifically, the two wavelengths remain indistinguishable and do not separate.

Table 12. Dichromatic Vision on Mars.

Epoch	$\lambda_{1max}$	$\lambda_{2max}$	mIoU
0	560.00	425.00	-
100	571.49	428.05	18.16
200	575.26	428.68	24.86
300	578.98	429.02	27.54
400	580.68	429.21	31.36
500	582.98	429.34	34.11
600	582.52	429.24	36.58
700	583.21	429.21	37.48
800	584.79	429.23	39.25
900	586.70	429.34	39.15
1000	588.81	429.37	41.53

Table 13. Trichromatic Vision on Mars.

Epoch	$\lambda_{1max}$	$\lambda_{2max}$	$\lambda_{3max}$	mIoU
0	588.81	588.81	429.37	-
100	596.48	584.76	431.02	16.44
200	603.89	580.89	432.35	23.79
300	609.40	576.38	433.12	26.22
400	615.76	573.13	434.03	29.77
500	621.05	573.67	434.30	32.71
600	625.98	574.24	434.57	35.30
700	630.70	575.09	434.83	36.38
800	637.33	577.62	435.22	37.77
900	642.24	579.63	435.55	39.14
1000	647.87	582.86	435.80	39.88

Similarly, we allow gene duplication to simulate the hypothetical evolutionary transition from trichromatic to tetrachromatic vision in the Martian environment, as illustrated in Tab.14.

Table 14. Tetrachromatic Vision on Mars.

Epoch	$\lambda_{1max}$	$\lambda_{2max}$	$\lambda_{3max}$	$\lambda_{4max}$	mIoU
0	647.87	647.87	582.86	435.80	-
100	646.60	644.15	577.73	434.19	18.62
200	647.90	643.76	576.71	434.22	26.45
300	648.76	643.28	575.91	434.24	29.72
400	649.90	643.35	575.27	434.32	30.44
500	651.01	643.49	574.80	434.37	34.62
600	651.91	643.63	574.44	434.45	34.78
700	653.35	644.21	573.90	434.63	36.20
800	654.66	644.73	573.73	434.80	35.51
900	655.83	645.11	573.14	434.82	39.33
1000	657.08	645.72	572.63	434.95	41.07

The quantitative results indicate that dichromatic vision achieves the best performance in the Martian envi-

ronment. This suggests that hypothetical Martian creatures may evolve to have dichromatic vision if the environmental conditions remain consistent.

## 9. Supplementary Results for Camera Design

In the main text, due to space limitations, we used the maximum sensitivity wavelengths of human opsins (580, 540 and 425 nm) as a baseline to initiate the training process for the opsin layer, effectively demonstrating the validity of our camera design strategy. In this section, we present additional potential camera designs to further demonstrate the versatility and broad applicability of our approach. Specifically, we explore camera designs with varying numbers of filters, each initialized with different wavelengths.

### 9.1. Camera for Martian Environment

In this section, we present the design of cameras with varying numbers of filters, optimized for operation in the Martian environment. As shown in Tab.15, R, G, and B represent the red, green, and blue colour filters, respectively. The initial parameters for the maximum sensitivity wavelengths of these filters are set to 590 nm, 540 nm, and 460 nm, respectively, aligning with the values commonly used in general cameras [47]. Therefore, we train various configurations of the opsin layer with learning rate  $3 \times 10^{-2}$  to obtain the colour response functions of filters optimized for the best segmentation performance. As shown in Tab.15, we propose specific camera filter designs. Additionally, our results demonstrate the potential for implementing minimalist designs for specialized cameras, utilizing the minimum number of filters required to achieve optimal performance.

Table 15. Camera Specialized for Martian Environment.

Filters	$\lambda_{1max}$	$\lambda_{2max}$	$\lambda_{3max}$	$\lambda_{4max}$	mIoU %
R	613.31	-	-	-	36.26
R/B	617.28	460.04	-	-	40.78
R/G	612.92	522.32	-	-	40.61
R/R/B	618.02	616.54	458.08	-	40.37
R/R/B/B	627.63	621.87	458.42	455.51	41.60

### 9.2. Camera for Cancer Detection

Similar to Sec.9.1, we train various configurations of the opsin layer to obtain the colour response functions of filters optimized for the best segmentation performance. As shown in Tab.16, we propose specific camera filter designs.

In addition, for the segmentation task, we replace the MiT encoder and segmentation decoder used previously with a U-Net model [52] featuring a ResNet-34 backbone [25] and a U-Net decoder, similar to the baseline model in [73]. The opsin layer is integrated into the U-Net architecture, and the opsin layer, backbone, and U-Net decoder are

Table 16. Camera Specialized for Cancer Detection.

Filters	$\lambda_{1max}$	$\lambda_{2max}$	$\lambda_{3max}$	$\lambda_{4max}$	mIoU %
R	607.46	-	-	-	53.33
R/B	614.47	473.57	-	-	54.26
R/G	618.32	532.17	-	-	54.33
R/R/B	623.49	618.05	479.86	-	52.79
R/R/B/B	638.06	639.55	486.83	486.16	53.98

trained simultaneously. As illustrated in Tab.17, we propose a 3-filter camera design optimized using the U-Net architecture, demonstrating that our evolutionary conservation optimization framework is robust and effective across different model architectures, including both transformer-based models with MiT encoders and convolutional architectures like U-Net.

Table 17. Results With U-Net Model.

Camera	$\lambda_{1max}$	$\lambda_{2max}$	$\lambda_{3max}$	Iou of cancer <sup>%</sup>
Standard	590.00	540.00	460.00	42.56
Design	602.29	535.06	455.12	44.42